Supplement of The Cryosphere, 14, 2267–2281, 2020
https://doi.org/10.5194/tc-14-2267-2020-supplement

The Cryosphere Open Access EGU

Supplement of

Satellite-observed monthly glacier and snow mass changes in southeast Tibet: implication for substantial meltwater contribution to the Brahmaputra

Shuang Yi et al.

Correspondence to: Shuang Yi (shuangyi.geo@gmail.com)

1. Supplementary figures and tables

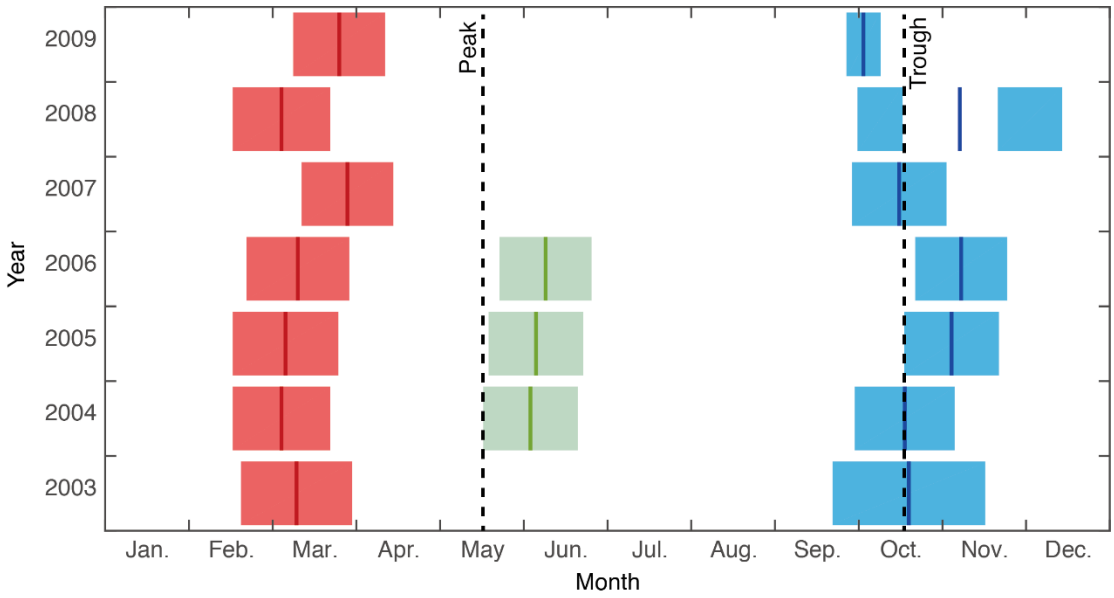

Figure S1. ICESat operational periods. The observations are categorized into three seasons. The middle of each period is taken as the observation time. The seasonal mass variations of glacier and snow in the SET based on GRACE have peak and trough values in May and in October, respectively.

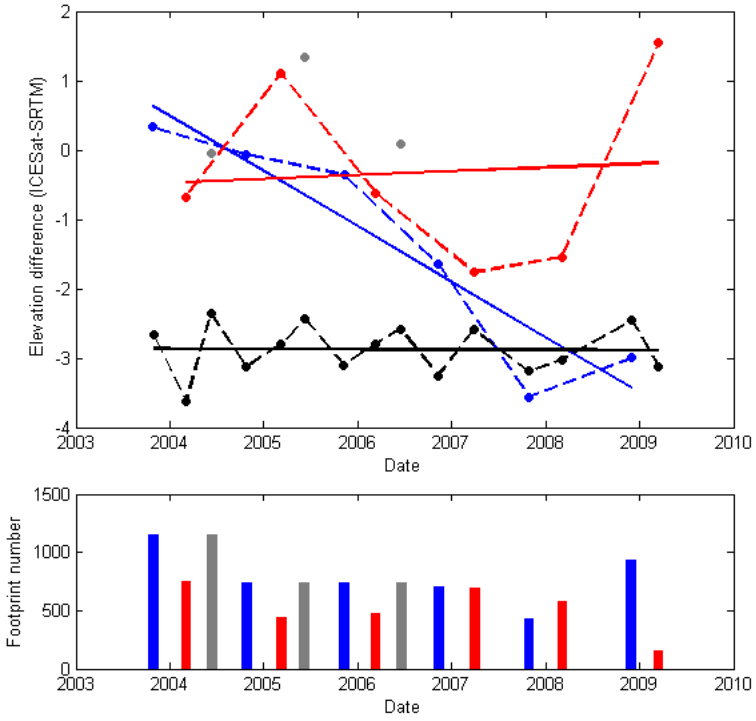

Figure S2. Surface height change of glaciers in the SET. (Top) Elevation difference of glaciers in October/November (blue), March (red) and June (gray). The black shows the result of a non-glacier region. (Bottom) The number of footprints. The result in 2009 has too few footprints and is not used.

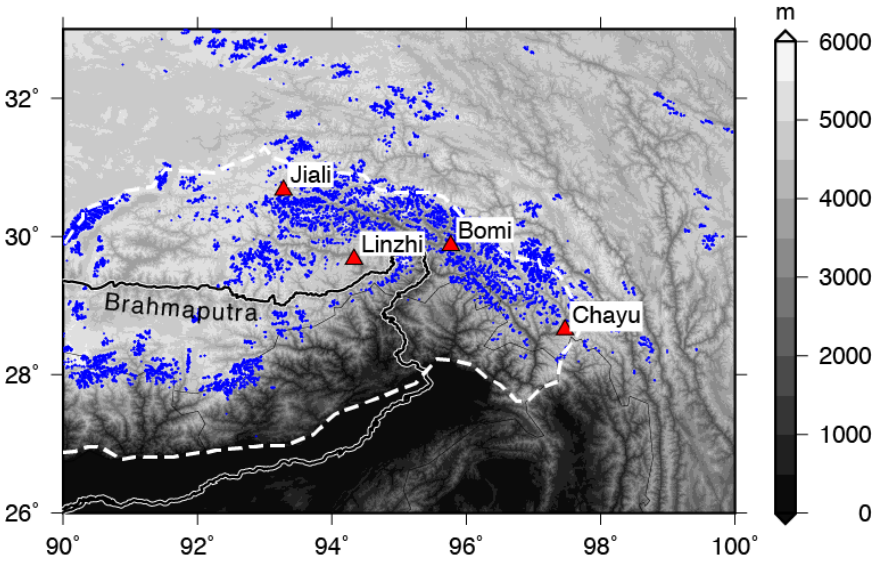

Figure S3. Locations of four meteorological stations in the study region. The gray background shows the topography, and the blue shaded areas represent the distribution of glaciers. The boundary of the upper Brahmaputra Basin is marked by the dashed white curve.

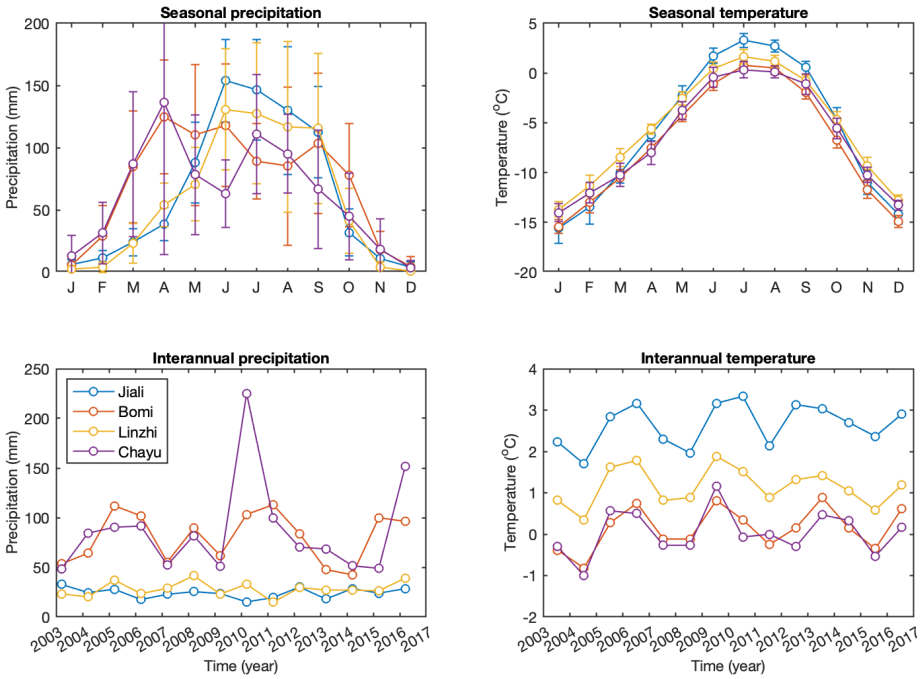

Figure S4. Seasonal and interannual changes in precipitation and temperature in the weather stations shown in Figure S3. The error bars show the dispersions among the years.

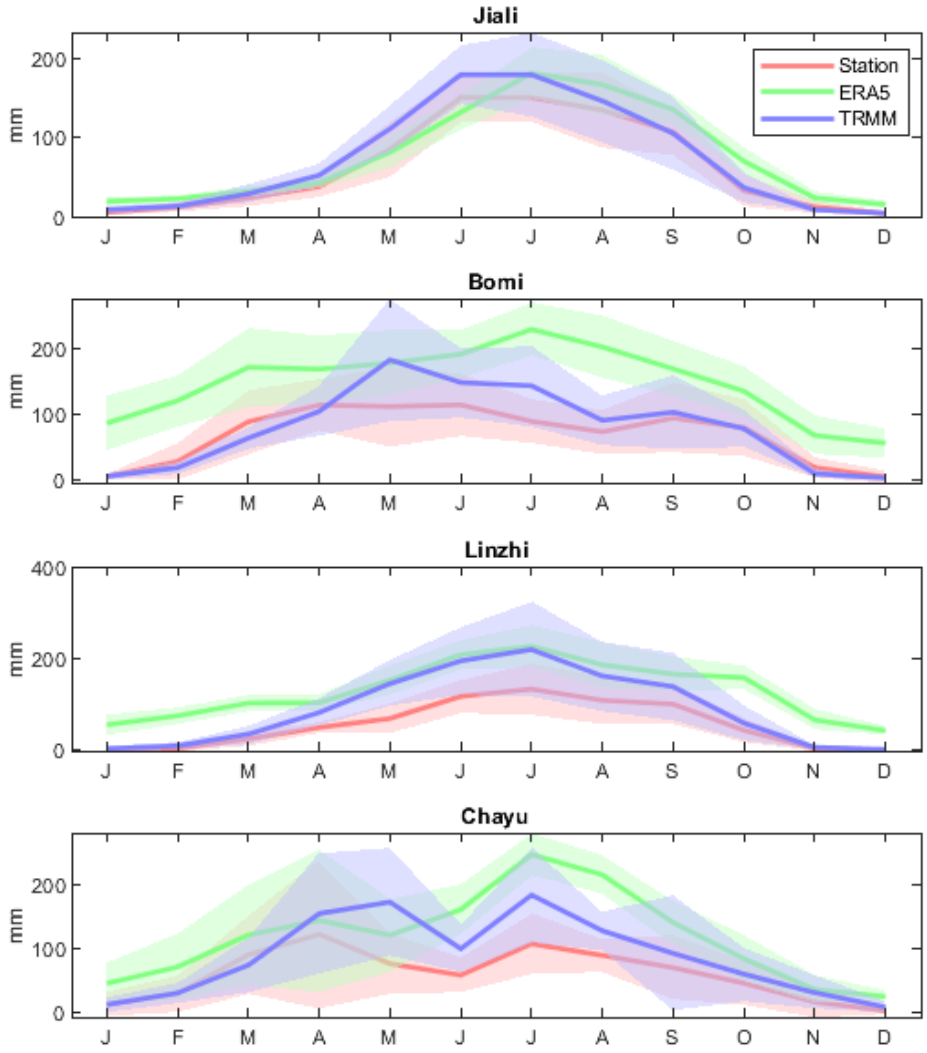

Figure S5. Comparison of seasonal precipitation results from meteorological stations, ERA5 and TRMM.

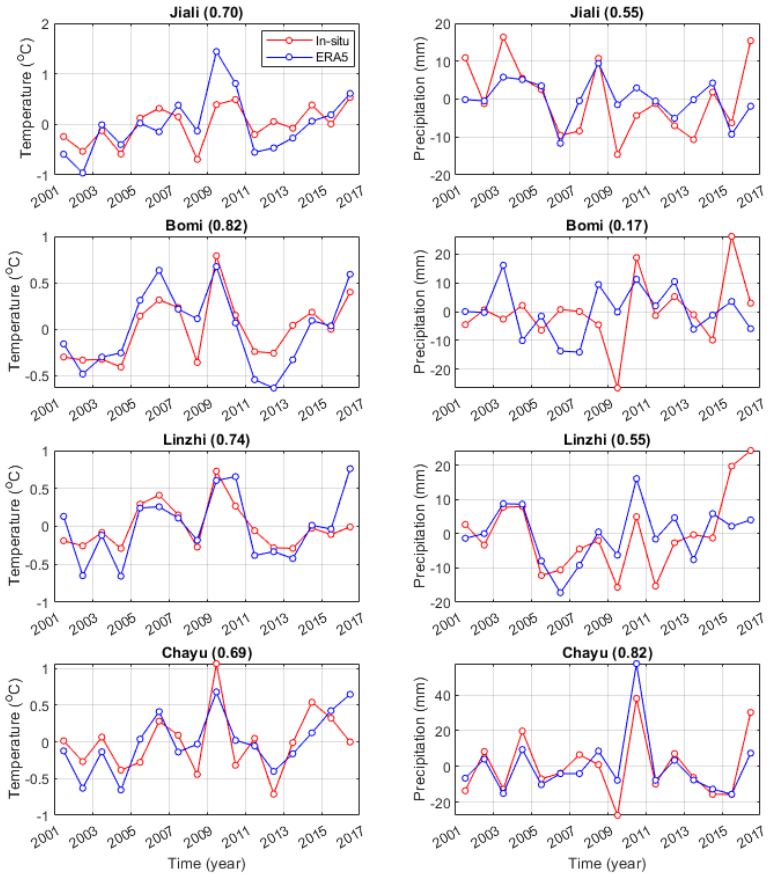

Figure S6. Comparison of annual temperature (left) and precipitation (right) records from ERA5 and in-situ observations. The correlation coefficient is given in the title. The mean value of the whole period is removed so only anomalies are shown here.

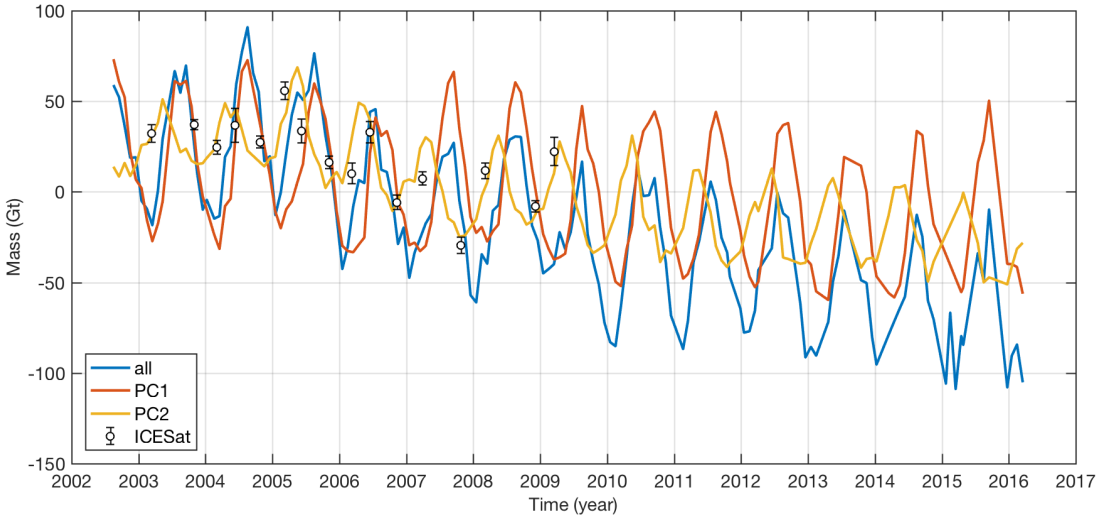

Figure S7. Mass estimates in the glacierized zone using the first two modes (PC1 and PC2) and the whole signal of GRACE (all).

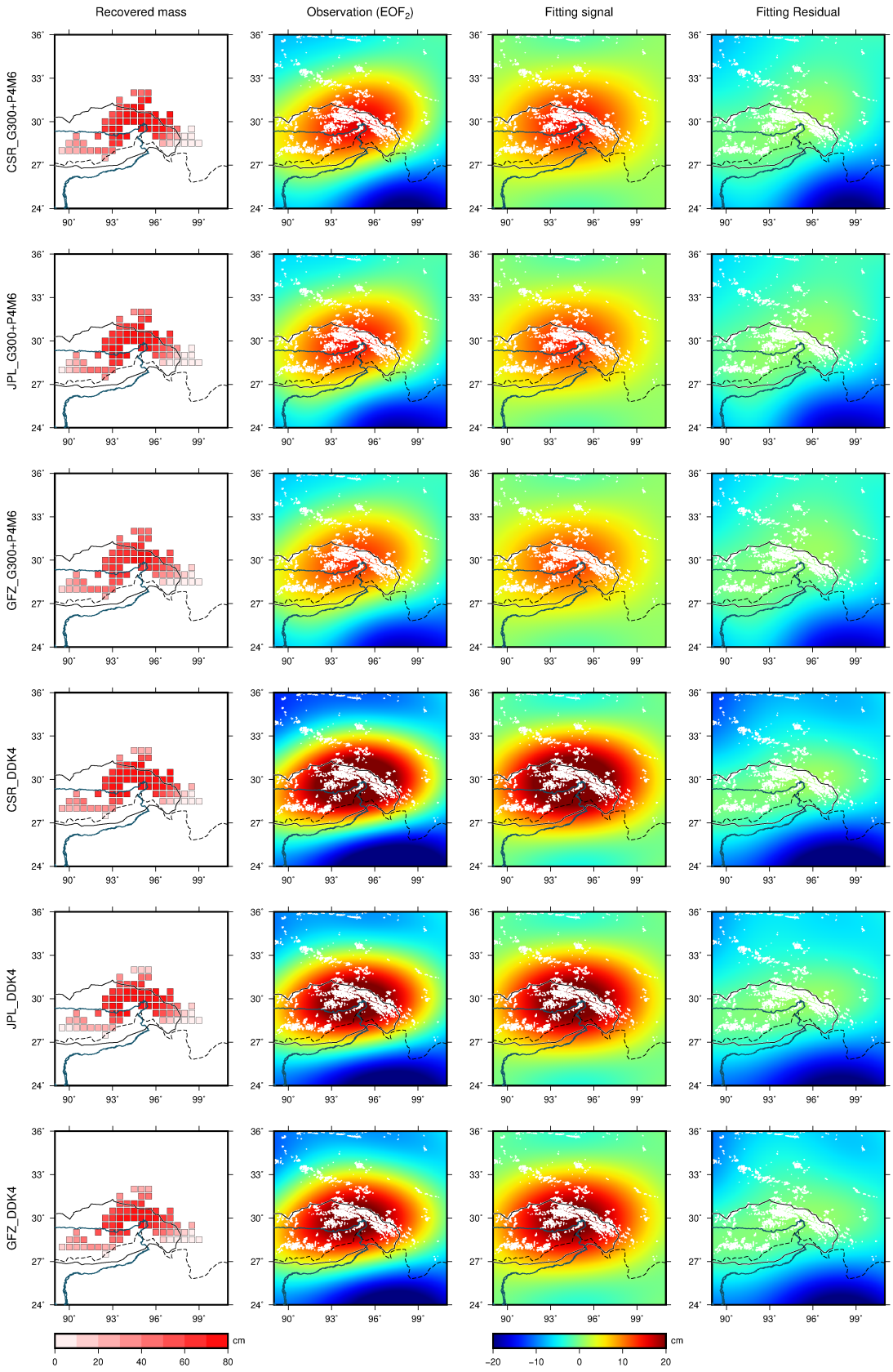

Figure S8. Recovered mass changes from the second EOF of different datasets and filters. The combination of each row is annotated to the left.

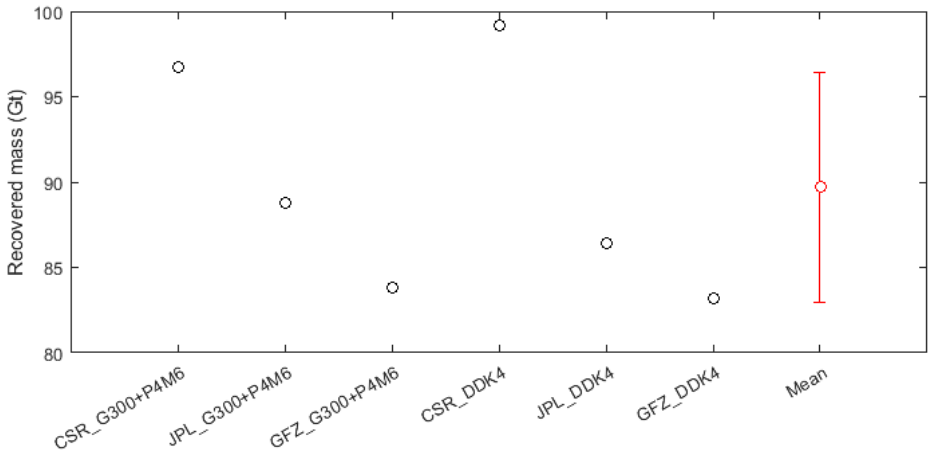

Figure S9. Recovered mass changes and their mean. The uncertainty is estimated based on the standard deviation.

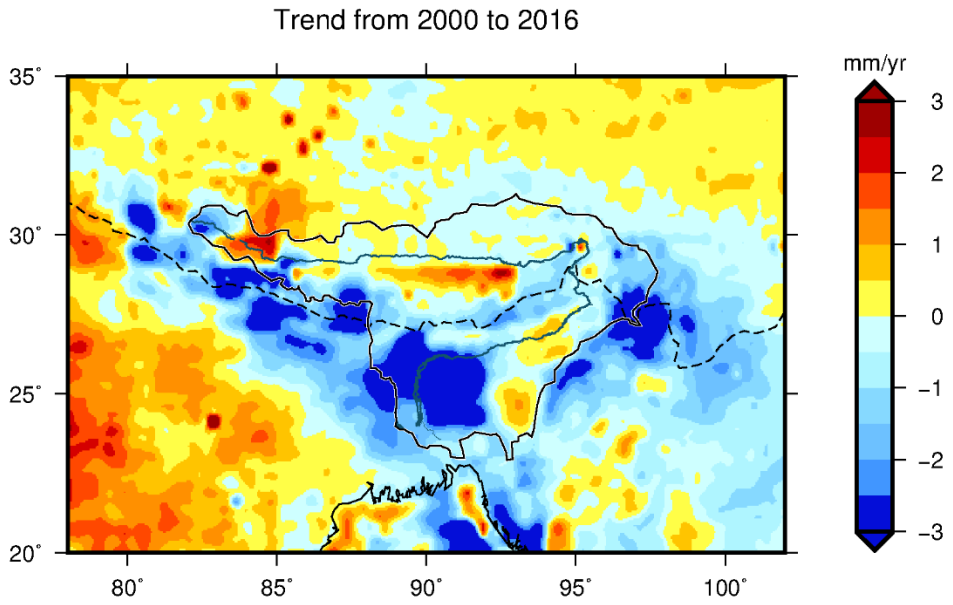

Figure S10. Trend of precipitation from 2000 to 2016 in the study region by using the TRMM product.

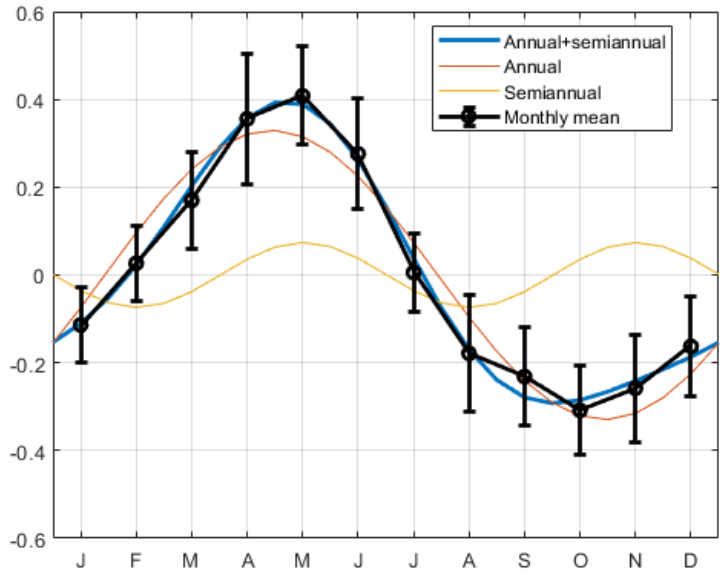

Figure S11. Constructed seasonal variation compared with GRACE PC_2 series (the black curve with error bars).

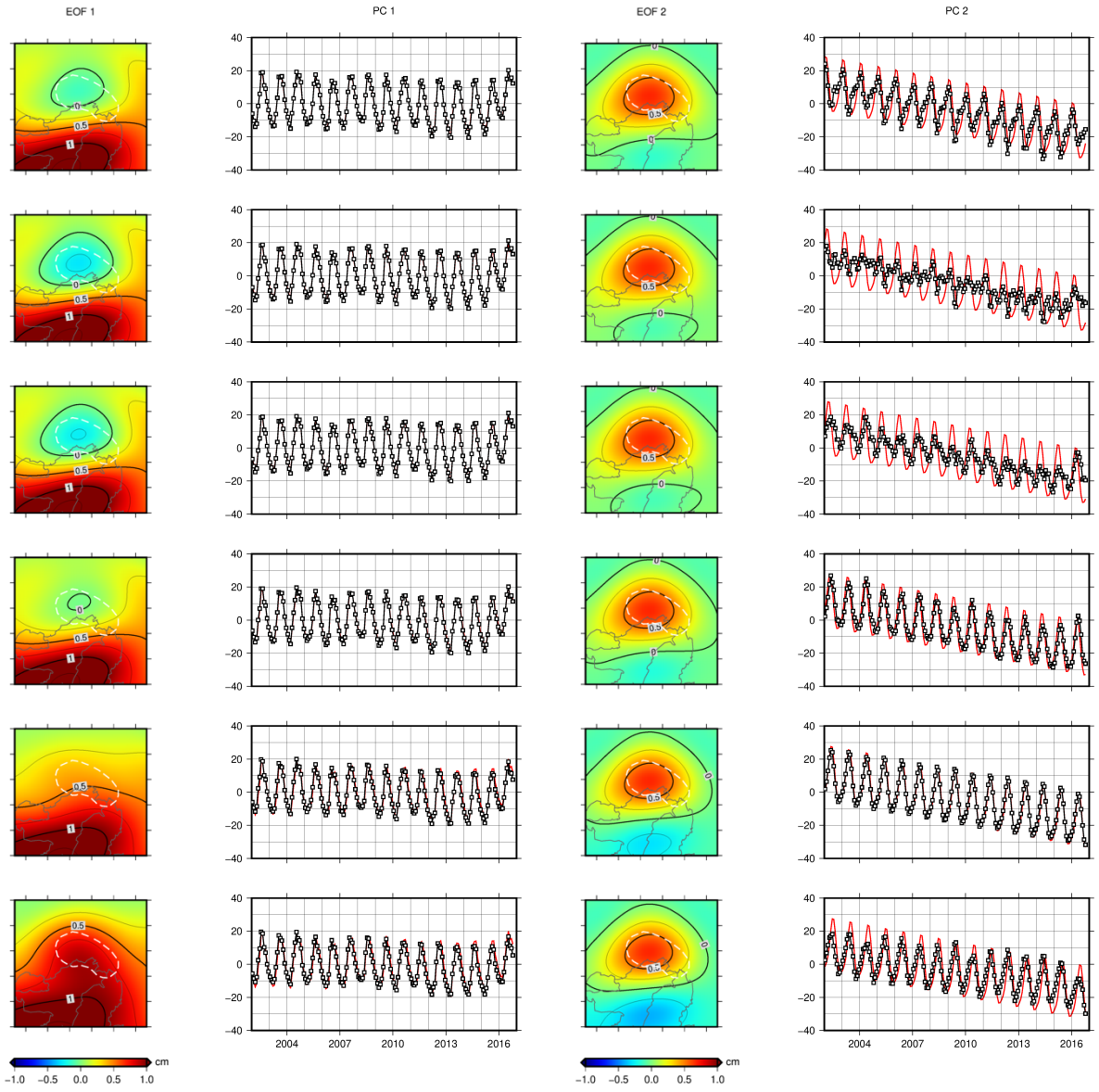

Figure S12. The first two modes of the EOF analysis of various mass simulations in the southeastern Tibet. The GS mass change has a peak month gradually shifting from January to June (from top to bottom). Refer to the text for the details about the models. The white dashed circle in each EOF plot roughly marks the glacierized area. The red curve in each PC plot shows the modeled series, and the black shows the PC.

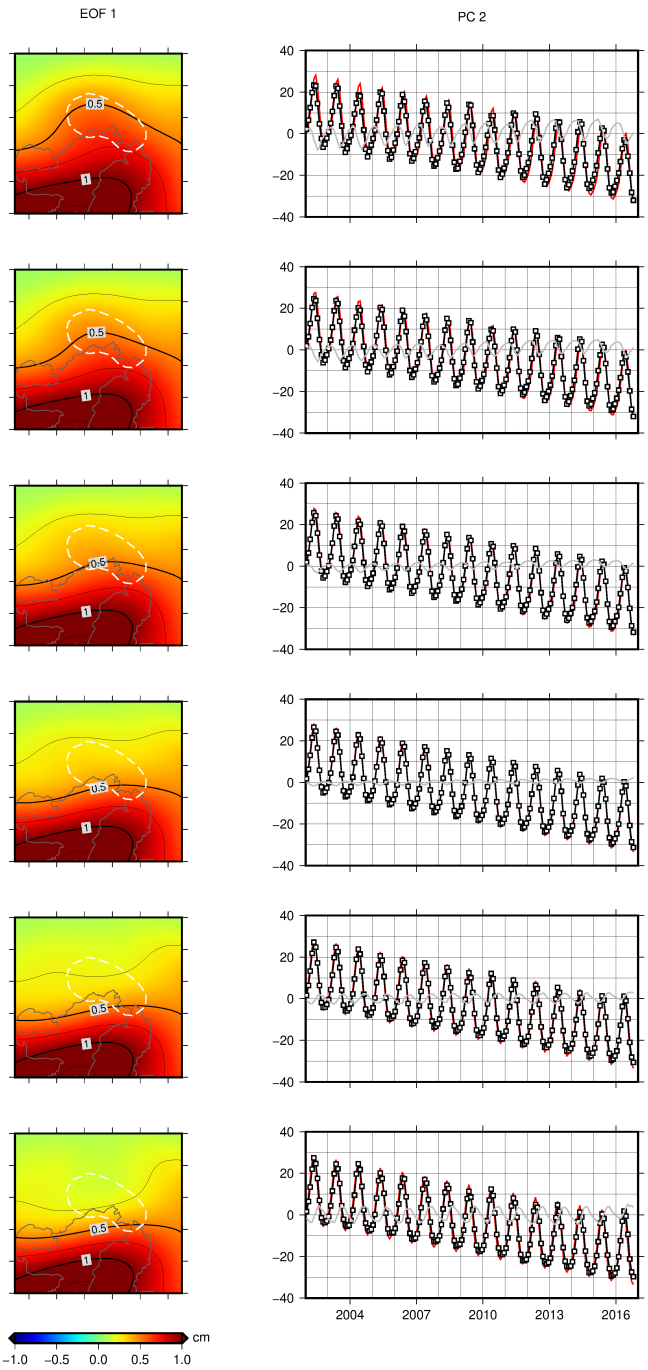

Figure S13. Same as Figure S12, but the peak date of glaciers is shifted from May 1st to May 26th by a 5-day interval (from top to bottom), and only EOF_1 and PC_2 are shown. The gray series in each PC plot show the difference of PC_2 relative to the modeled value.

Table S1. Geographic information of four meteorological stations.

Station	Longitude	Latitude	Elevation
Jiali	93.28	30.67	4488.8
Bomi	95.77	29.87	2736.0
Linzhi	94.33	29.67	2991.8
Chayu	97.47	28.65	2327.6

2. Introduction of EOF

Generally, geophysical observations in the *i*th time epoch span a two-dimensional range, but they can be reorganized into a column vector $X_{.,i}$ (n grids). These column vectors during the whole study period (t epochs) can form a matrix X with size $n \times t$. In the second step, singular value decomposition (SVD) method can be adopted to find orthogonal bases in the spatial and temporal domains:

$$X = USV',$$

where both U and V are orthonormal matrixes. S is a diagonal matrix and its diagonal elements are singular values of X. The matrix X is decomposed into N modes:

$$X = \sum_{i=1}^{N} U_{.,i} \times s_i \times V'_{.,i},$$

where $N = \min(n,t)$ and s_i is the *i*th diagonal element of S. The *i*th mode is composed of three items. Here, $U_{.,i} \times s_i$ is defined as the *i*th EOF (named EOF*i*) and $V_{.,i}$ is defined as the *i*th principal component (named PC*i*). EOF*i* can be rearranged back to the spatial distribution which the original observations ($X_{.,i}$) have. Then, EOF*i* and PC*i* represent the spatial feature and the temporal evolution of the *i*th mode, respectively. For a better readability, PC*i* is rescaled by a factor of a to make its maximum absolute value equals 1, and EOF*i* is rescaled correspondingly by a factor of $1/a$ so that the *i*th mode remains unchanged.

Since both variations of $U_{.,i}$ and $V_{.,i}$ are ones, s_i represents the explained variation of the *i*th mode:

$$\mathrm{EV}i = s_i^2 / \sum_{i=1}^{N} s_i^2 .$$

Because *s* is already in the descending order due to features of the SVD method, the EV is then also in the descending order, which means that the first modes explain the majority of the observations. Due to this characteristic, the EOF technique is often used to reduce the data amount and/or to improve the signal-noise-ratio by discarding the higher modes (Hannachi et al., 2007; Wouters and Schrama, 2007). In this study, the EOF method is used to separate gravity signals respectively caused by liquid and solid water, as they have different spatial domains (vast compared with local) and seasonal variations (an interval of three months in their peak months).

All EOFs/PCs are mathematically orthogonal to each other, and their geophysical explanation should be made with caution. Only limited modes can be explained by geophysical processes and one process may influence several modes (Eom et al., 2017). In this study region, terrestrial water storage change is the dominant source for seasonal gravity change so it's likely to be reflected in the first mode. We compare EOF1 and PC1 of GRACE observations with these from soil moisture (GLDAS/NOAH) and precipitation (TRMM), and the good resemblance confirms that the first mode of GRACE observations is caused by terrestrial water storage change.

3. Discussion on the orthogonality

3.1. peak month difference at the scale of months

The orthogonality lies in the fact that the GS signal peaks exactly in May, which is not confirmed by other observations. We do find that the PC_2 of GRACE observations reaches a peak value in May, but it may be caused by our EOF analysis. Therefore, we conduct various GS mass modeling to test whether the orthogonality is artificial. Only water storage change and GS mass change are considered in the numeric modeling. The water storage change is obtained directly from the first mode of the decomposition of the GLDAS/NOAH model, and the GS mass change *m* is determined by an annual and semiannual variations and a linear trend, as shown the equation below:

$$m_i = Acos\left(\frac{2\pi}{T} \times (t - \varphi_i)\right) + A'cos\left(\frac{2\pi}{T'} \times (t - \varphi_i')\right) + at,$$

where t is the observation time, a is the trend, A, φ, and T are the amplitude, phase and period of the annual variation, and these with apostrophe represent corresponding variables for the semiannual variation. The peak month φ_i is gradually shifted from January to June (if the GS mass reaches the maximum between July and December, then it contradicts the ICESat observation). Based on the relative magnitude between the first two modes in the EOF analysis of GRACE, the amplitude A and trend a are determined to be 16 cm w.e. and -1 cm w.e. yr^{-1}, respectively. The semiannual variation is determined beforehand to construct a seasonal variation with fast decrease and slow increase: $\varphi_i' = \varphi_i + 1\,month$, and A'=0.22*A. Therefore, there are six models. An example of the constructed seasonal variation is compared with the GRACE PC_2 series in Figure S12, which shows that the simulated annual and semiannual variations can fit the seasonal component in our observations well.

The result is shown in Figure S12. The first mode composed by EOF_1 and PC_1 represents water storage change and the second composed by EOF_2 and PC_2 represents GS mass change. The red curves in the PC plots represent the modeled series, and their consistency with the decomposed series (the black curves) demonstrates the effectivity of our method. Two conclusions can be made. First, only in the case of May can we fully restore the GS mass change (i.e., a good agreement between the red and the black curves). Second, The PC_1 and EOF_2 are insensitive to the shift in month, while EOF_1 and PC_2 are sensitive. Besides, EOF_1 and PC_2 are always coupled so EOF_1 can be used to evaluate whether the PC_2 is well restored, or whether a leakage happens. If a leakage happens, an abnormal bulge can be identified in the glacierized zone (marked by the white dash circle) in EOF_1. This bulge shows how the compensation from the hydrological signal distorts its spatial pattern. In fact, the bulge exists in all cases except May. If we look back at Figure 3 in the manuscript, we can find the EOF_1 of GRACE does not have such a bulge, which indicates that the GS signal can only peak in May and that the leakage from the hydrological signal is little, even if it exists.

Here, the orthogonality maintains if the GS peaks in November, but it is unrealistic

for three reasons. First, it implies that the GS accumulates in summer and autumn, and melts in winter and spring, which is unlikely to happen in the northern hemisphere. Second, if it is realistic, it means that the PC_2 series should be multiplied by -1 (so it peaks in November), but it simultaneously inverts the long-term mass loss to mass increase, and GS mass increase contradicts current observations. Third, the ICESat observation clearly shows that glacier surface elevation is higher in the first half of the year.

3.2. peak month difference at the scale of weeks

As we have shown above, the glacier mass change peaks in May. We can only determine the month without the exact day of the month due to the temporal resolution of GRACE. However, a time shift in weeks may slightly deteriorate the temporal orthogonality, so a moderate leakage can still take place. We model glacier mass change on different days in May to investigate this possibility. The peak month is shifted from May 1st to May 26th by a 5-day interval and the result of EOF_1 and PC_2 is shown in Figure S13. In the glacierized zone, the bulge gradually decreases from May 1st and reaches a minimum in May 11th, and turned negative afterwards. By comparing with the EOF_1 of GRACE (Figure 3), we can identify that the real glacier mass change is possible to have a peak date ranging from May 6th to May 16th (the bulge is too evident in other cases), and this time range is used for leakage error estimation. Based on the results of modelled and recovered glacier mass change, their residuals may have a trend of up to 9% and a seasonal variation of up to 11% of the modeled glacier mass change. These values are used to estimate the leakage error.

4. Precipitation integration

The mathematical expression of precipitation integration is

$$IntP(j) = [\sum_{i=1}^{N} P(j-i+1) * W(N-i+1)] \,/\, \sum_{i=1}^{N} W(i),$$

where *IntP* represents the integrated precipitation in the *j*th month, *P* is short for precipitation, *W* is the weight matrix for the integration, and *N* is the integration window.

The key parameters are *N* and *W*. In Fig. S13, we tried three schemes. (upper), $N = j$, $W(i) = 1$; (middle), $N = 4$, $W = [0.4,0.6,0.8,1]$; (below), $N = 6$, $W = [1,2,3,4,5,6]$. The first scheme is cumulative precipitation. This one does not work well, because it assumes the impact of precipitation in this month is the same as that in months ago, which is not reasonable. The second and the third schemes similarly have a gradually increasing weight function, but the third one has a longer integration window. We find the difference in window length and slight change of weight matrix puts few effects on the interannual variation, but impacts the agreement in the seasonal variation. The third scheme is used in this study.

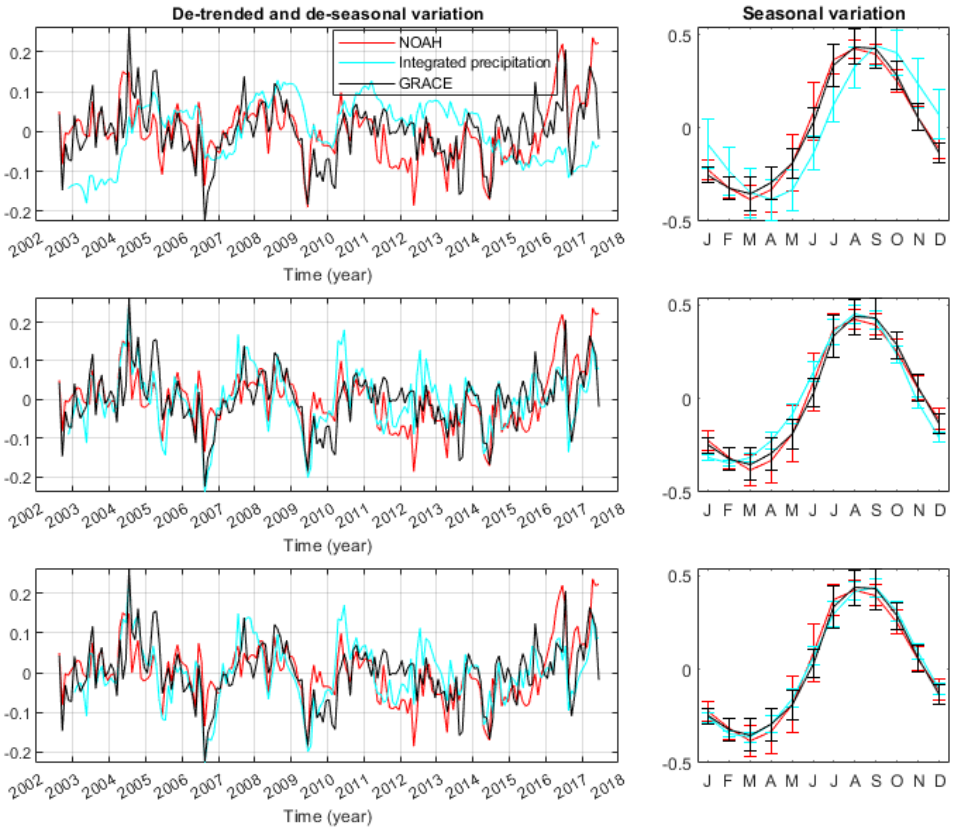

Figure S13. Different methods for precipitation integration.

5. Reference

Eom, J., Seo, K.-W., Ryu, D., 2017. Estimation of Amazon River discharge based on EOF analysis of GRACE gravity data. Remote Sensing of Environment, 191: 55-66. DOI:10.1016/j.rse.2017.01.011

Hannachi, A., Jolliffe, I.T., Stephenson, D.B., 2007. Empirical orthogonal functions and related techniques in atmospheric science: A review. International Journal of Climatology, 27(9): 1119-1152. DOI:10.1002/joc.1499

Wouters, B., Schrama, E.J.O., 2007. Improved accuracy of GRACE gravity solutions through empirical orthogonal function filtering of spherical harmonics. Geophysical Research Letters, 34(23): n/a-n/a. DOI:10.1029/2007gl032098